ACS PHYSICAL CHEMISTRY Au
AN OPEN ACCESS JOURNAL OF THE AMERICAN CHEMICAL SOCIETY

pubs.acs.org/physchemau
Article

Tailor-Made Design of Three-Dimensional Batteries Using a Simple, Accurate Geometry Optimization Scheme

Kaito Miyamoto*

Cite This: ACS Phys. Chem Au 2024, 4, 546−554
Read Online
ACCESS | Metrics & More | Article Recommendations | Supporting Information

ABSTRACT: In the rapidly evolving Internet of Things (IoT) society, the demand for microbatteries with high areal energy density is surging. As a promising strategy to enhance areal energy density, three-dimensional (3D) batteries have attracted attention. The feature of 3D batteries is the decoupling of the electrode thickness from the ion-transport distance through the modification of the spatial arrangement of the positive and negative electrodes beyond the conventional parallel plates configuration. This allows for the accommodation of a larger amount of active materials without increasing internal resistance. However, identifying the optimal 3D geometry is a complex task, as it depends on printable materials, the resolution of the fabrication equipment, as well as battery usage, which constitutes a multiobjective optimization problem. To overcome this challenge, we propose a novel approach to determine the optimal 3D microbattery geometry. Our innovative method involves a 3D battery optimization system, which integrates an automatic geometry generator with a quick and accurate performance simulator. This approach allows, for the first time, the discovery of material- and discharge-current-dependent optimal geometries. We successfully apply this optimization scheme to two standard electrode pairs ($LiFePO_4$/$Li_4Ti_5O_{12}$ and $LiNi_{0.5}Mn_{0.3}Co_{0.2}O_2$/graphite), demonstrating a significant increase in energy density (30%−40% greater than the current state-of-the-art geometry), particularly under high current conditions. These findings underscore the importance of tailor-made batteries for diverse IoT applications and showcase the potential of our approach in realizing such designs.

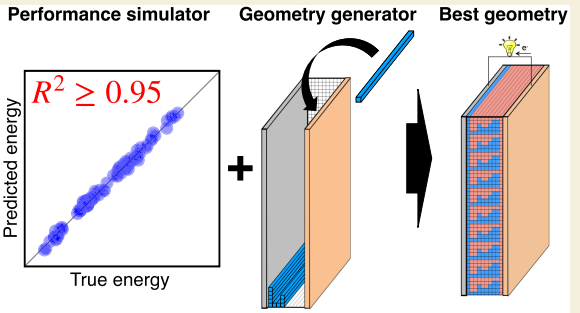

KEYWORDS: *lithium-ion batteries, 3D microbatteries, electrode design, optimization, machine learning, multiobjective optimization, regression models*

INTRODUCTION

The proliferation of the Internet of Things (IoT) society, driven by advancements in information and communications technology (ICT) and the miniaturization of electronic devices and sensors, has necessitated the development of smaller devices in various fields such as mobility, housing, and healthcare. In this context, microbatteries, which are comparable or smaller in size to these miniaturized devices, have emerged as a critical component for their off-grid operation.[1,2] While thin-film microbatteries have been developed and commercialized,[3] they suffer from a low areal energy density (1 mWh/cm^2),[4] which restricts their application to IoT devices or limits the devices' functionality. Increasing the thickness of the electrodes can increase the theoretical capacity; however the resulting longer ion-transport distance prevents access to the added materials during operation (Figure 1A), thereby not improving the areal energy density for practical applications.[4,5] This highlights the importance and need for further research and development in the field of microbatteries.

To enhance the areal energy density of microbatteries, one promising strategy is to decouple the electrode thickness and the ion-transport distance.[4,6] This can be achieved by designing the spatial arrangement of the positive and negative electrodes three-dimensionally without using the conventional parallel plates configuration. Microbatteries having such electrodes are called three-dimensional (3D) microbatteries.[6−8] One example of such batteries is the interdigitated electrodes configuration shown in Figure 1B and, the figure clearly shows that the configuration realizes the decoupling of the electrode thickness and the ion-transport distance. To date, various fabrication technologies for 3D batteries, such as lithography[9,10] and additive manufacturing,[11,12] have been proposed and demonstrated.[2,9,13−19]

The common limitation of the 3D battery fabrication technologies is that the range of the printable materials is constrained by these methods.[20] As the shape of the optimal 3D electrodes depends on the used materials generally, the

Received: May 16, 2024
Revised: July 1, 2024
Accepted: July 3, 2024
Published: July 16, 2024

https://doi.org/10.1021/acsphyschemau.4c00039
ACS Phys. Chem Au 2024, 4, 546−554

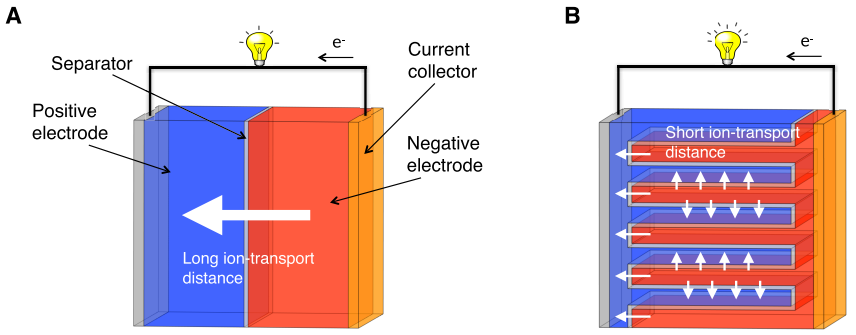

Figure 1. Comparison of conventional and 3D batteries. (A) Conventional battery with thick electrodes (parallel plates configuration). (B) One example of the 3D batteries (interdigitated electrodes configuration).

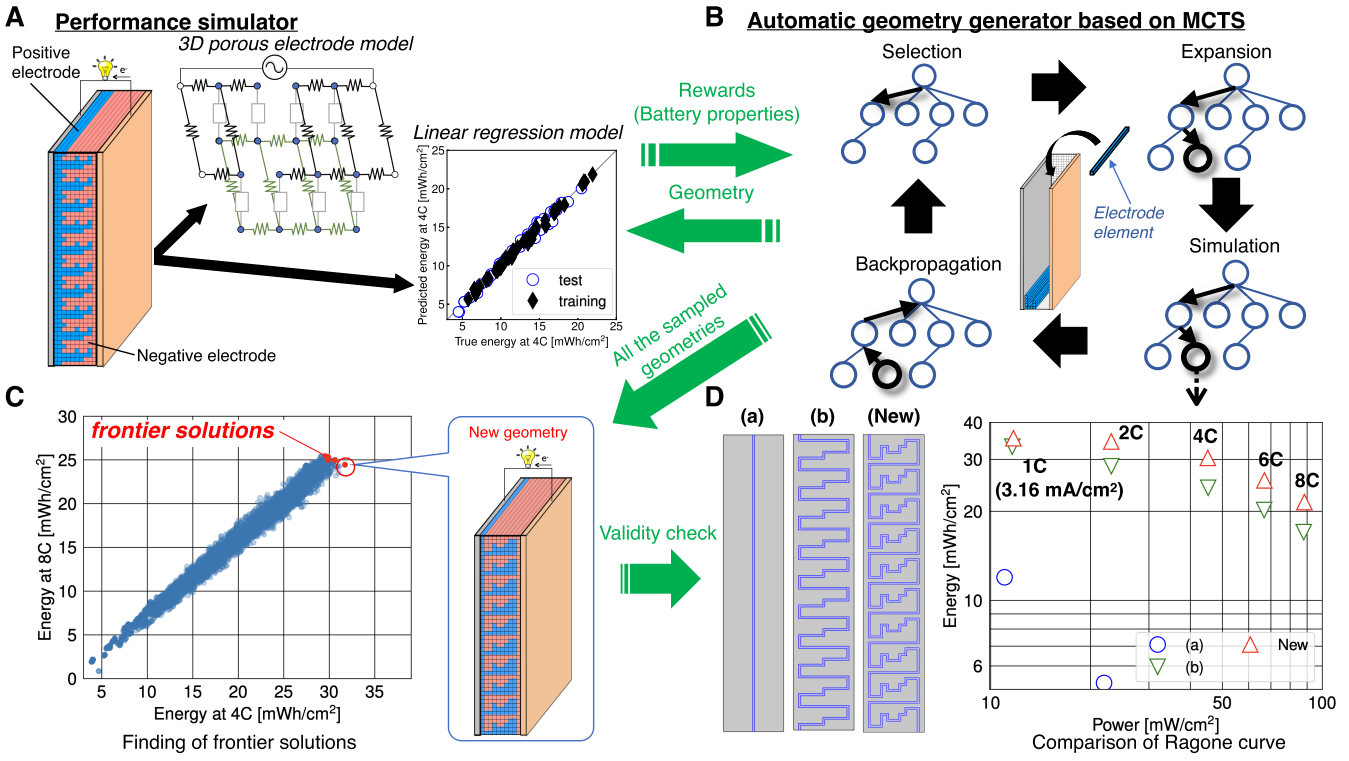

Figure 2. 3D battery optimization scheme utilizing a quick and accurate performance simulator and automatic geometry generator. In this example, 3D batteries that display high areal power and energy densities are designed. (A) Performance simulator examples, including a three-dimensional porous electrode model and a linear regression model for calculating energy density. (B) Automatic geometry generator based on Monte Carlo tree search (AGG-MCTS), which generates high-performance battery geometries based on rewards calculated by the performance simulator. (C) Energy distribution of 3D batteries generated by AGG-MCTS, and identification of the highest-performance batteries (frontier solutions). (D) Validation of the highest-performance batteries. Here, the geometry named "New" corresponds to the front side of the new geometry shown in panel (C), and this geometry remains the same in the depth direction.

geometry should be optimized every time when new materials and fabrication technology are used. Moreover, given that microbatteries are used in a wide range of IoT devices, optimizing their performance to meet specific requirements is crucial. This primarily involves choosing between a high-power or high-energy orientation, essentially focusing on the optimization of the Ragone curve.[15] However, this constitutes a multiobjective optimization problem, posing significant challenges even when computer simulations are employed due to their high computational cost.[21] Indeed, there have been no reports that address such an optimization problem.

In this paper, we tackle this problem by extending our simple 3D battery optimization system.[22−24] Our approach automatically designs the spatial arrangement of the positive and negative electrodes by combining an automatic geometry generator with a performance simulator, where the areal energy density is computed quickly and accurately using an electrochemistry-based regression model. As the newly proposed regression models utilize an internal resistance that depends on both materials and current condition as one of the features for prediction, accurate prediction of energies for optimal geometries that lie in the extrapolation region is possible. We successfully demonstrate the effectiveness of the method by finding material- and discharge-current-dependent optimal geometries for the first time.

https://doi.org/10.1021/acsphyschemau.4c00039
ACS Phys. Chem Au 2024, 4, 546−554

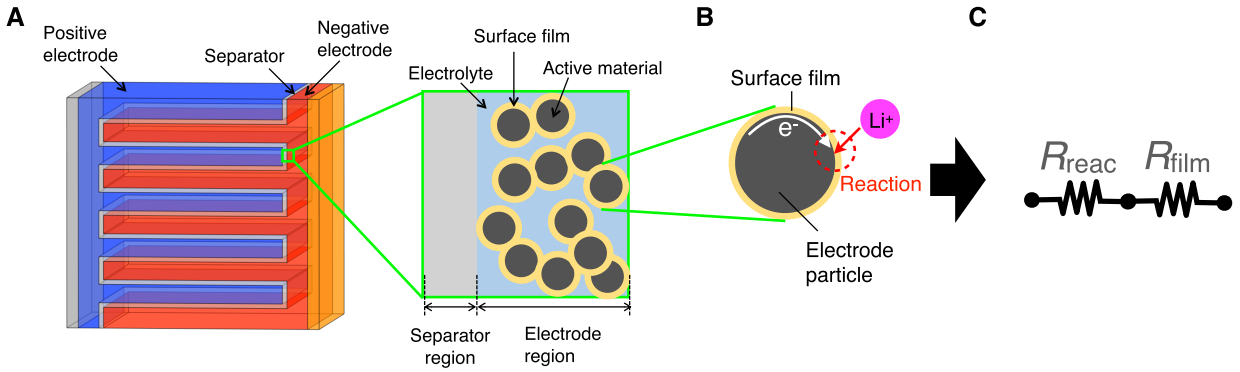

Figure 3. Definition of the charge transfer resistance used in 3D-PEM. (A) Example of the 3D battery and its enlarged diagram of the interface between the negative electrode and the separator. Usually, the lithium-ion battery uses porous electrodes. Thus, the electrode region consists of both electrolyte and electrode materials. (B) Schematic diagram of the charging reaction at the interface between the electrolyte and the negative electrode particle. (C) Charge transfer resistance is modeled by the serial connection of the reaction resistance (R_{reac}) and film resistance (R_{film}).

METHODS

The 3D Battery Optimization System

We briefly summarize our 3D battery optimization system and optimization protocol with an example shown in Figure 2. Our optimization system consists of two key technologies: a performance simulator (Figure 2A), and an automatic geometry generator based on Monte Carlo tree search (AGG-MCTS) shown in Figure 2B.

The performance simulator computes the battery properties quickly and accurately. This includes a transmission line model named the three-dimensional porous electrode model (3D-PEM) for impedance calculations[22] and principal component regression (PCR) models to predict energies.[23] We demonstrated that PCR models successfully predict energies of 3D batteries with R^2 values of greater than 0.92 and internal resistance computed by 3D-PEM plays an important role as a feature of the models to achieve high accuracy.[23]

AGG-MCTS creates feasible 3D battery architectures without relying on human intuition and experience for the spatial arrangement of electrodes. As shown in Figure 2B, each geometry is formed by filling the vacant cell with cuboid-shaped electrodes (electrode elements). Since the size of the electrode elements is determined following the resolution of the fabrication technologies such as 3D printers, only fabricatable geometries can be generated. In the current implementation of AGG-MCTS, only 3D batteries with two degrees of freedom in electrode design are generated, as illustrated in Figure 2. This means that only the frontal geometry is optimized, and this geometry remains the same in the depth direction. We have introduced this restriction due to feasibility concerns. Specifically, at present, 3D printing is the only possible method to develop intricate 3D batteries, but this technology is currently limited to creating 2D patterned batteries,[16,17] such as the interdigitated electrodes configuration shown in Figure 1B. We have demonstrated that such 2D geometric designs significantly impact battery performance.[22−24] The detailed algorithm of AGG-MCTS is described in the Computational Details section of the Supporting Information.

Figure 2 illustrates the process of finding optimal geometries that achieve both high power and high energy densities as an example. Initially, energy prediction models are developed (as shown in Figure 2A). Using these models, AGG-MCTS generates 3D battery geometries, taking into account their performance (Figure 2B). Subsequently, as depicted in Figure 2C, all sampled geometries are plotted to identify the optimal ones, known as frontier solutions. The optimization process is completed by validating these optimal geometries. This is done by drawing the Ragone plot through continuum simulations, or experiments if feasible (Figure 2D).

The effectiveness of our approach was demonstrated by automatically designing a set of 3D battery geometries that have both high areal power and energy densities, where lithium manganese oxide (LMO) spinel and graphite (Osaka Gas MCMB 25−10)[25] as the active materials in the positive and negative electrodes, respectively.[23,24] Indeed, only our approach realized optimization of an entire battery cell although many simulation-based 3D battery optimizations have been reported,[21,26−34] i.e., all of the previous works reported optimization of only the dimensions of the interdigitated or pillar electrode,[27−33] or the simplified battery cell.[34]

The limitation of our optimization system described in refs22−24. is that resistivity parameters used in 3D-PEM are determined based on the Nyquist plots, assuming a battery system is in an equilibrium state. Thus, nonlinearity in the charge-transfer resistance is not included in the model. As microbatteries are used under high current conditions, errors in computed internal resistance by 3D-PEM ($R_{inter}^{3D\text{-}PEM}$) may become substantial due to the nonlinear effect. In addition, from our previous study,[23] we confirmed that $R_{inter}^{3D\text{-}PEM}$, when used as a descriptor (feature), significantly contributes to the accuracy of the energy prediction models. Thus, there is a potential risk of decreasing accuracy in the energy prediction model if the error in $R_{inter}^{3D\text{-}PEM}$ is large. As the magnitude of the error stemming from the nonlinearity depends on the current condition as well as used materials, it is mandatory to include such effect to the model for maintaining the generality of our approach, leading to the successful discovery of material- and discharge-current-dependent optimal geometries. Therefore, this problem is tackled in this paper.

The Three Dimensional Porous Electrode Model

Internal resistance is a fundamental property that strongly influences the charging and discharging behavior of batteries. Thus, quick and accurate evaluation of the internal resistance of the 3D batteries is of importance. This has motivated us to devise 3D-PEM, which is a natural extension of the conventional transmission line model.[22]

In 3D-PEM, the battery cell is divided into finite elements; and an electric circuit is formed by linking the centers of these elements using impedances as illustrated in Figure S1 of the Supporting Information. Since the electric circuit is designed based on the shape of the electrodes, this approach enables the incorporation of geometric effects into the evaluation of cell impedance.

Current Dependent Charge-Transfer Resistivity. In 3D-PEM, ionic resistivity (ρ_{ion}), electronic resistivity (ρ_e), and charge-transfer resistivity (ρ_{ct}) are necessary as input parameters to compute the internal resistance. Among them, ρ_{ion} and ρ_e are computable easily from experimentally determined materials' property parameters, that are merely reciprocals of the ionic and electronic conductivities of the composite electrode, respectively.[23] As for ρ_{ct}, as mentioned earlier, the value was computed based on the Nyquist plots under a battery system in an equilibrium state.[22,23] Thus, current condition dependency stemming from the nonlinear effect is not considered. In addition, the relationship between ρ_{ct} and materials parameters was unclear. Therefore, in this study, we propose a new approach to compute ρ_{ct} directly from materials parameters and a current condition.

Figure 3 shows a schematic diagram of electrode reactions in a three-dimensional battery. Figure 3A illustrates an example of the three-

https://doi.org/10.1021/acsphyschemau.4c00039
ACS Phys. Chem Au 2024, 4, 546−554

dimensional battery and an enlarged view of the interface between the negative electrode and the separator. It is noteworthy that we assume porous electrodes for both positive and negative electrodes. Thus, the electrode reaction takes place at the interface between an active material and an electrolyte in the electrode region. Also, a surface film is assumed on the active materials as the film dominates the battery performance, e.g., the solid electrolyte interphase (SEI) on the graphite anode.[35] During the operation, lithium ions pass through the surface film then reaction takes place on the electrode particle as illustrated in Figure 3B. Therefore, the charge transfer resistance can be modeled as the series connection of reaction resistance (R_{reac}) and film resistance (R_{film})

$$R_{ct} = R_{reac} + R_{film} \tag{1}$$

as shown in Figure 3C. In 3D-PEM, R_{ct} is represented using the charge-transfer resistivity ρ_{ct} [Ωcm^3] and electrode volume V as $R_{ct} = \rho_{ct}/V$.[22] Thus, R_{reac} and R_{film} can also be represented by

$$R_{reac} = \frac{\rho_{reac}}{V} \tag{2}$$

$$R_{film} = \frac{\rho_{film}}{V} \tag{3}$$

where ρ_{reac} and ρ_{film} denote reaction resistivity and film resistivity, respectively. Here, V is the volume of the electrode region in Figure 3A, which includes not only the volume of electrode particles but also that of the electrolyte.

As for ρ_{film} evaluation, a film resistance per unit reaction surface area (ρ_{film}^{area} [Ωcm^2]) is provided as a material property parameter.[25] Thus, R_{film} is computed by

$$R_{film} = \frac{\rho_{film}^{area}}{A_{reac}} \tag{4}$$

where A_{reac} denotes the reaction surface area. From the comparison of eq 4 and eq 3, we obtain

$$\rho_{film} = \rho_{film}^{area}\frac{V}{A_{reac}} \tag{5}$$

Thus, if we know the ratio between electrode volume and reaction surface area, we can obtain ρ_{film}. If we assume the shape of the active materials as a sphere, which is a common assumption in the field of battery simulations,[25] $A_{reac} = 3\epsilon_s V/r_s$. Thus,

$$\rho_{film} = \frac{r_s}{3\epsilon_s}\rho_{film}^{area} \tag{6}$$

where ϵ_s and r_s represent the volume fraction of active materials and the radius of the active material, respectively. Throughout this paper, we use eq 6 to evaluate ρ_{film}.

R_{reac} is computable by taking the derivative of activation overpotential η with respect to electric current at the interface between the active materials and electrolyte (I), i.e., $R_{reac} = d\eta/dI$. R_{reac} can be computable analytically if reaction kinetics is represented by the Butler–Volmer equation with the transfer coefficients of 0.5 as

$$I = I_0\left(\exp\left(\frac{F}{2RT}\eta\right) - \exp\left(-\frac{F}{2RT}\eta\right)\right) \tag{7}$$

where I_0, F, R, and T represent exchange current, Faraday constant, gas constant, and temperature, respectively.

As $\sinh x = (e^x - e^{-x})/2$, this equation can be transformed into

$$\frac{I}{I_0} = 2\sinh\frac{F}{2RT}\eta \tag{8}$$

Then, the inverse function of eq 8 is given by

$$\eta = \frac{2RT}{F}\ln\left(\frac{1}{2}\frac{I}{I_0} + \sqrt{\frac{1}{4}\left(\frac{I}{I_0}\right)^2 + 1}\right) \tag{9}$$

By taking the derivative of eq 9 with respect to I, we obtain R_{reac} as

$$R_{reac} = \frac{d\eta}{dI} = \frac{RT}{FI_0}\frac{1 + \frac{I}{2I_0\sqrt{\frac{1}{4}\left(\frac{I}{I_0}\right)^2 + 1}}}{\frac{I}{2I_0} + \sqrt{\frac{1}{4}\left(\frac{I}{I_0}\right)^2 + 1}} \tag{10}$$

If we assume that interfacial current density is constant regardless of the location within the electrode, I equals to the charge or discharge current of the battery (I_{ext}). Thus, using $I_0 = i_0 A_{reac}$ where i_0 denotes the exchange current density, we arrive at

$$R_{reac} = \frac{RT}{Fi_0A_{reac}}\frac{1 + \frac{I_{ext}}{2I_0\sqrt{\frac{1}{4}\left(\frac{I_{ext}}{I_0}\right)^2 + 1}}}{\frac{I_{ext}}{2I_0} + \sqrt{\frac{1}{4}\left(\frac{I_{ext}}{I_0}\right)^2 + 1}} \tag{11}$$

From the comparison of eq 11 and eq 2, ρ_{reac} is obtained as

$$\rho_{reac} = \frac{RT}{Fi_0}\frac{V}{A_{reac}}\frac{1 + \frac{I_{ext}}{2I_0\sqrt{\frac{1}{4}\left(\frac{I_{ext}}{I_0}\right)^2 + 1}}}{\frac{I_{ext}}{2I_0} + \sqrt{\frac{1}{4}\left(\frac{I_{ext}}{I_0}\right)^2 + 1}} = \rho_{reac}^{LFA}\frac{1 + \frac{I_{ext}}{2I_0\sqrt{\frac{1}{4}\left(\frac{I_{ext}}{I_0}\right)^2 + 1}}}{\frac{I_{ext}}{2I_0} + \sqrt{\frac{1}{4}\left(\frac{I_{ext}}{I_0}\right)^2 + 1}} \tag{12}$$

where ρ_{reac}^{LFA} is the reaction resistivity when the Butler–Volmer equation is linearized, an approximation known as the low field assumption (LFA).[36] If the shape of the active materials is a sphere, ρ_{reac}^{LFA} becomes

$$\rho_{reac}^{LFA} = \frac{RT}{Fi_0}\frac{r_s}{3\epsilon_s} \tag{13}$$

From the comparison between eqs 12 and 13, it is clear that ρ_{reac} depends on I_{ext} while ρ_{reac}^{LFA} does not.

As $R_{ct} = \rho_{ct}/V$ by definition,[22] the charge-transfer resistivity can be computed using

$$\rho_{ct} = \rho_{film} + \rho_{reac} \tag{14}$$

Here, it is noteworthy that we derived the analytical form to compute ρ_{reac} by assuming the Butler–Volmer equation with the transfer coefficients of 0.5 (eq 7). However, ρ_{reac} is also computable by taking the derivative of η with respect to I numerically as long as I and η are available. Such an approach is especially effective when the analytical form of ρ_{reac} cannot be obtained.

To investigate the consistency of this approach with our previous parameter determination method, i.e., the method based on the Nyquist plot,[22,23] we computed ρ_{ct} of the negative electrode using the materials parameters and discharge-current conditions (i.e., low current condition of 3.16 mA/cm^2 and high current condition of 12.64 mA/cm^2) specified in ref 23. Using this approach, ρ_{ct} is calculated to be 1.001 Ωcm^3 (the sum of ρ_{film} of 0.9731 and ρ_{reac} of 0.0278) and 1.000 Ωcm^3 (the sum of ρ_{film} of 0.9731 and ρ_{reac} of 0.0269) at low and high current conditions, respectively. These values are nearly identical to the value in ref 23., which is 1.000 Ωcm^3. Also, from this comparison, we find that nonlinear effect in ρ_{ct} is negligibly small under the materials and discharge-current conditions used in ref 23.

Since the 3D-PEM operates as a simple electric circuit, computing its internal resistance is quick. This rapid computation enables the use of internal resistance as an important feature for accurately predicting the energy of the 3D battery during optimization in our scheme (Figure 2).

RESULTS AND DISCUSSION

Accuracy of Internal Resistance Computed Using 3D-PEM

To investigate the accuracy of the 3D-PEM, the internal resistance ($R_{inter}^{3D\text{-}PEM}$) of the 3D battery is compared with that

https://doi.org/10.1021/acsphyschemau.4c00039
ACS Phys. Chem Au 2024, 4, 546−554

Table 1. Comparison of the Internal Resistance for the 3D Battery Shown in Figure S2 in the Supporting Information, Using LFP and LTO as Positive and Negative Electrode Active Materials[a]

	ρ_{film} [Ω cm^3]		ρ_{reac} [Ω cm^3]				
C rate	LFP	LTO	LFP	LTO	$R_{inter}^{3D\text{-}PEM}$ [Ω]	R_{inter}^{CM} [Ω]	Error [%]
1	0.0000	0.0000	0.3649	0.0134	615.9	692.6	11.1
2	0.0000	0.0000	0.1978	0.0134	525.1	603.4	13.0
3	0.0000	0.0000	0.1340	0.0133	486.3	552.9	12.0
4	0.0000	0.0000	0.1011	0.0133	464.1	519.9	10.7
LFA	0.0000	0.0000	0.8189	0.0134	837.6	817.1	2.5

[a]1C current corresponds to 3.16 [mA/cm^2]. LFA represents the results when the low-field assumption is used to compute ρ_{reac}. The LFA value for R_{inter}^{CM} is computed from the onset of the discharge curve at 0.001C.

Table 2. Comparison of the Internal Resistance of the 3D Battery Shown in Figure S2 in the Supporting Information, Where NMC532 and GR Are Selected As Active Materials for the Positive and Negative Electrodes[a]

	ρ_{film} [Ω cm^3]		ρ_{reac} [Ω cm^3]				
C rate	NMC532	GR	NMC532	GR	$R_{inter}^{3D\text{-}PEM}$ [Ω]	R_{inter}^{CM} [Ω]	Error [%]
1	0.0083	0.0400	0.0062	0.0448	128.9	126.8	1.7
4	0.0083	0.0400	0.0062	0.0412	126.5	124.6	1.5
8	0.0083	0.0400	0.0061	0.0337	121.4	120.6	0.6
LFA	0.0083	0.0400	0.0062	0.0451	129.1	126.9	1.7

[a]Results are presented as in Table 1.

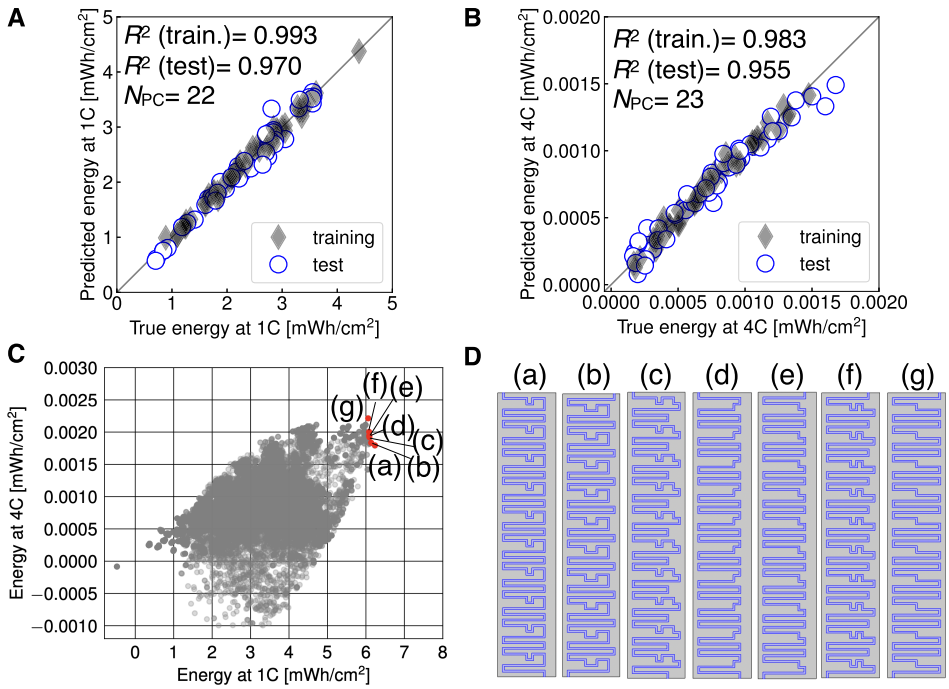

Figure 4. Results of optimization for the LFP/LTO system. (A) Comparative analysis of true versus model-predicted energy values at 1C. (B) Comparative analysis of true versus model-predicted energy values at 4C. (C) Energy distribution of geometries sampled using AGG-MCTS for 1C and 4C (20,869 geometries), where frontier solutions are colored in red. (D) Geometries of the frontier solutions, where (a) − (g) correspond to those in panel (C). Here, black diamond and blue open circle in panels (A) and (B) represent training and test data; R^2 (train.) and R^2 (test) represent R^2 values of training and test data, respectively. Also, N_{PC} represents the number of principal components to construct the regression model. 1C indicates the current of 3.16 mA/cm^2 in this paper (see Computational Details section in the Supporting Information). In panel (D), the blue color represents the 20 μm thick separator and the left and right sides of the separator are positive and negative electrodes, respectively.

from continuum simulations (R_{inter}^{CM}). Here, we should note that R_{inter}^{CM} is computed from the polarization of the battery cell (the difference between the cell voltage and the open-circuit voltage) at the onset of discharge to disregard diffusion resistance as the current implementation of 3D-PEM does not take into account this effect. As for the geometry, the intricate 3D battery shown in Figure S2 in the Supporting Information is selected. This geometry was generated in ref 23., using an automatic geometry generator based on a randomized algorithm under the condition that the volume ratio of the positive and negative electrode is 1:1, corresponding to the geometry 1 in Figure S3 of ref 23. To compute $R_{inter}^{3D\text{-}PEM}$, the system is divided into 150 × 30 elements and, then, the transmission line model is constructed by connecting the centers of the elements.

https://doi.org/10.1021/acsphyschemau.4c00039
ACS Phys. Chem Au 2024, 4, 546−554

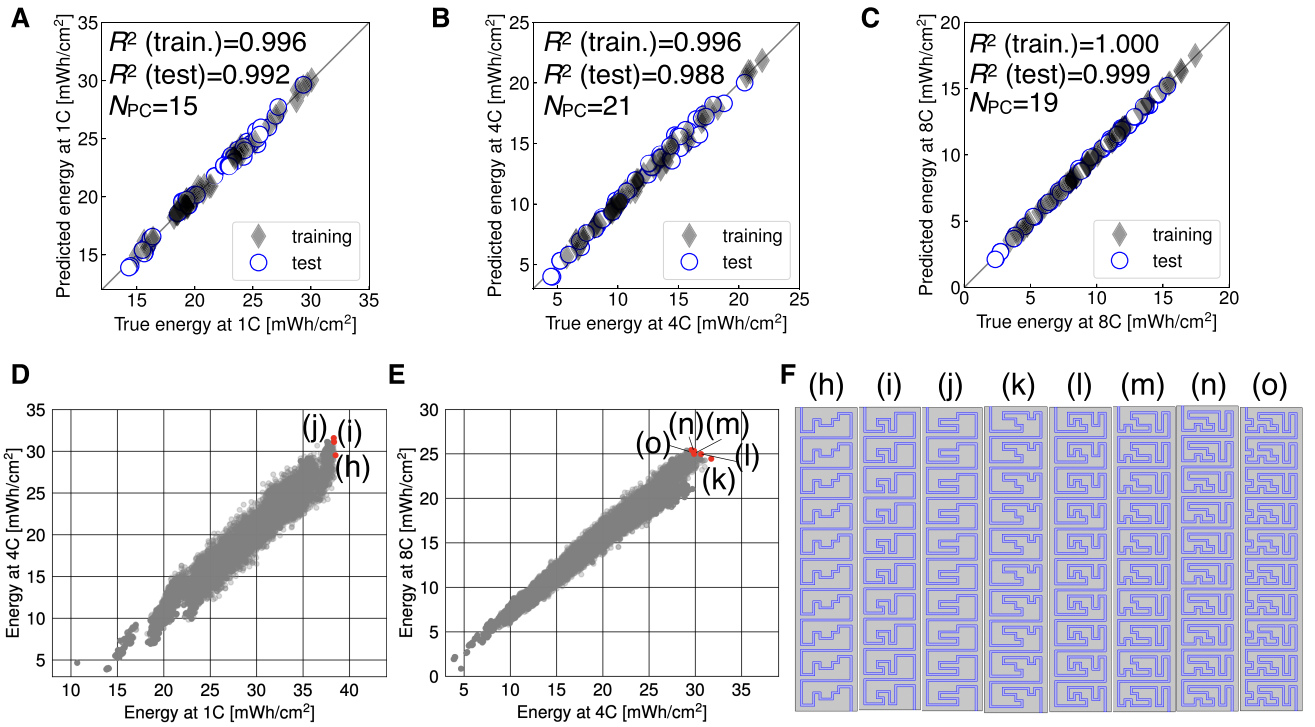

Figure 5. Results of optimization for the NMC532/GR system. (A) Comparative analysis of true versus model-predicted energy values at 1C. (B) Comparative analysis of true versus model-predicted energy values at 4C. (C) Comparative analysis of true versus model-predicted energy values at 8C. (D) Energy distribution of geometries sampled using AGG-MCTS for 1C and 4C, where frontier solutions are colored in red. (E) Energy distribution of geometries sampled using AGG-MCTS for 4C and 8C, where frontier solutions are colored in red. (**F**) Geometries of the frontier solutions, where (h) − (o) correspond to those in panels (D) and (E). Total number of geometries sampled using AGG-MCTS is 32,732 geometries, that are used to create panels (D) and (E). Data are plotted as in Figure 4.

For the battery system, we selected systems utilizing LFP/LTO and NMC532/GR as active materials. These combinations are chosen because they are standard, yet their discharge behaviors are distinctly different.[5] Here, LFP, LTO, NMC532, and GR refer to $LiFePO_4$, $Li_4Ti_5O_{12}$, $LiNi_{0.5}Mn_{0.3}Co_{0.2}O_2$, and graphite, respectively. Corresponding resistivity parameters are summarized in Tables S4 and S5 in the Supporting Information. Other computational conditions can be found in the Computational Details section of the Supporting Information.

Table 1 summarizes resistivity parameters (ρ_{film} and ρ_{reac}) as well as internal resistance for the LFP/LTO system. As this system does not have the film resistance, ρ_{ct} equals to ρ_{reac}. From the comparison between ρ_{reac} values of positive and negative electrodes, the reaction resistivity of the positive electrode is always greater regardless of the current density and shows a significant dependence on the current. This result reflects the difference in the rate constant (k in Table S1 of the Supporting Information). Furthermore, the decrease in ρ_{reac} with increasing current indicates that the impact of the reaction resistance to the battery property is greater at lower currents.

As for the internal resistance, $R_{inter}^{3D\text{-}PEM}$ decreases with the increase of the current and the value using LFA differs significantly compared with the current-dependent values (the error of greater than a few hundred Ω). This trend agrees well with that of R_{inter}^{CM}. The results indicate that the inclusion of the nonlinear effect in ρ_{reac} is vital to compute $R_{inter}^{3D\text{-}PEM}$ for this system.

As the error of $R_{inter}^{3D\text{-}PEM}$ relative to R_{inter}^{CM} is only 2.5% with LFA approximation, the error of around 10% for the current-dependent $R_{inter}^{3D\text{-}PEM}$ values mainly comes from the approximation of the nonlinear term in ρ_{reac} (i.e., assumption of the uniform interfacial current density). However, the error of 10% is still considered to be small for the approximative model, and it is possible to use the model for the optimization.[37]

Table 2 summarizes resistivity parameters and internal resistance for the NMC532/GR system. In this system, both ρ_{reac} values and their current dependence are smaller than those for the LFP/LTO system. Thus, in contrast to the LFP/LTO system, the current dependence on $R_{inter}^{3D\text{-}PEM}$ is small and, interestingly, LFA becomes a good approximation. We confirm the excellent agreement between $R_{inter}^{3D\text{-}PEM}$ and R_{inter}^{CM}.

3D Battery Optimization Using AGG-MCTS

3D battery optimizations are conducted for both the LFP/LTO and NMC532/GR systems following the protocol illustrated in Figure 2. To directly compare the performance of the optimized geometries with those in the previous work,[24] optimization conditions, such as the dimensions of the battery geometry and design resolution, are taken from ref 24. The PCR models to predict energies are combined with AGG-MCTS to optimize 3D batteries. From a couple of energies under different current conditions, the shape of the Ragone curve is predicted. Detailed computational conditions can be found in the Computational Details section of the Supporting Information.

The LFP/LTO System. Optimization results for the LFP/LTO system are summarized in Figure 4. Figure 4A and Figure 4B show the performance of the energy prediction models at 1C and 4C. R^2 values are greater than 0.955, meaning our regression models accurately predict the energies by continuum simulations. Here, we should note that R^2 values of test data for 1C and 4C are 0.88 and 0.86 respectively if only $R_{inter}^{3D\text{-}PEM}$ and

https://doi.org/10.1021/acsphyschemau.4c00039
ACS Phys. Chem Au 2024, 4, 546−554

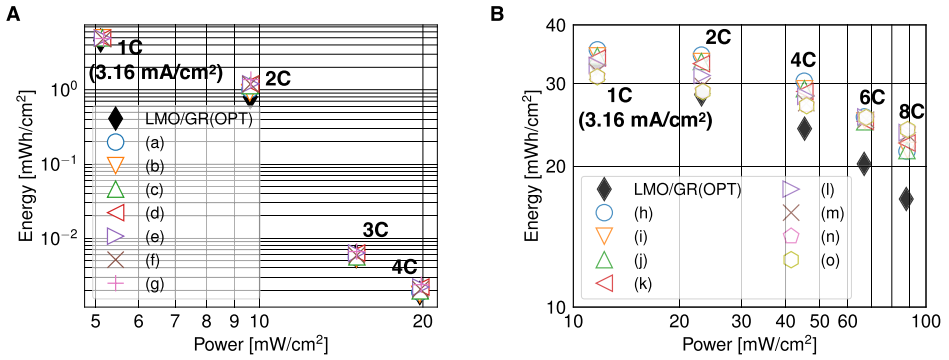

Figure 6. Performance comparison of optimal geometries and reference geometries. (A) Ragone plot of the optimal 3D batteries for the LFP/LTO system. (B) Ragone plot of the optimal 3D batteries for the NMC532/GR system. LMO/GR(OPT) represents the results of the optimal geometry for the LMO/GR system (see Figure S6 in the Supporting Information).

volume-scaled $R_{inter}^{3D\text{-}PEM}$ are used. This indicates that $R_{inter}^{3D\text{-}PEM}$ plays a major role in the accuracy of the regression model.

The energies of all the geometries sampled using AGG-MCTS (around 20,800 geometries) are plotted in Figure 4C and frontier solutions (a) − (g) are found. As is clear from Figure 4D, frontier solutions have similar geometrical features that they are composed of two types of electrode teeth: one with a constant width of 40 μm and another where the width varies, taking on either 40 or 100 μm. Interestingly, the geometrical features are different from the optimized geometries for the LMO/GR system,[24] a representative of those is shown in Figure S6 in the Supporting Information.

The NMC532/GR System. Figure 5 summarizes optimization results for the NMC532/GR system. Figure 5A, Figure 5B, and Figure 5C show the performance of the energy prediction models for 1C, 4C, and 8C, respectively. Excellent agreement between predicted and true values is confirmed (R^2 of greater than 0.988).

Energy distribution of the sampled geometries for 1C and 4C, and that for 4C and 8C are presented in Figure 5D and Figure 5E, respectively. As a result, frontier solutions (h) − (o) in Figure 5F are confirmed. Overall, electrode teeth widen as they get closer to the opposite current collector for this system. However, the optimal shape becomes more complex as the discharge current increases. This geometrical feature is completely different from both the LMO/GR system[24] and the LFP/LTO system.

Tables 1 and 2 demonstrated that $R_{inter}^{3D\text{-}PEM}$ strongly depends on the applied current due to the nonlinear effect in ρ_{reac} (eq 12). Thus, we investigate the contribution of such effect to the accuracy of the regression models. Figures S7 and S8 summarize the accuracies of the regression models constructed using the same features as those used to create the regression models in Figures 4 and 5, except for $R_{inter}^{3D\text{-}PEM}$, which is computed using LFA. From the comparison between Figure 5 and Figure S8, we do not observe a reduction in accuracy due to LFA regardless of the current condition. This is understandable considering the fact that the nonlinear effect is small for the NMC532/GR system, as shown in Table 2. Regarding the LFP/LTO system, from the comparison between Figure 4 and Figure S7, while the accuracy of the regression model at 1C remains unchanged, a drastic reduction in the R^2(test) value for the LFP/LTO at 4C (from 0.955 in Figure 4B to 0.855 in Figure S7B) is confirmed. This reduction corresponds to approximately twice the root-mean-square error (RMSE) for the test data, increasing from an RMSE of 8.51×10^{-5} mWh/cm^2 to 15.26×10^{-5} mWh/cm^2. This result is consistent with the observation from Table 1, where the nonlinear effect is the largest for the LFP/LTO system at 4C. Moreover, the error in Figure S7B increases with the magnitude of the energy. This indicates that including the nonlinear effect is vital for quantitatively predicting the energy of high-performance batteries during optimization. Here, it is noteworthy that although the accuracy of the regression models did not change, except for the LFP/LTO system at 4C, predicting the error due to the nonlinear effect on regression accuracy is difficult. Thus, including this effect is compulsory from the viewpoint of the generality of the optimization method.

Accuracy of the Regression Models for Optimal Geometries. The search for optimal geometries inherently involves an extrapolation problem, since these geometries are expected to lie outside the data region used for constructing the regression models (the extrapolation region). Property prediction in the extrapolation region is generally challenging using the regression model, thus, we have investigated the accuracy of the energy prediction models for the optimal geometries.

Predicted and true energies for the LFP/LTO system and the NMC532/GR system are summarized in Tables S6 and S7 in the Supporting Information, respectively; and those data are plotted along with the training and test data in Figures S9 and S10 in the Supporting Information. As is clear from Figures S9 and S10, the optimal geometries lie in the extrapolation region, however the regression models well predict the energies of the optimal geometries. All the models exhibited the prediction error of less than 9%, except for the energy at 1C for the LFP/LTO system. As for the energy at 1C for the LFP/LTO system, the model successfully captures the relationship between the geometry and energy even for the extrapolation region although the prediction accuracy is slightly worse than the other models with the average error of around 24%.

Although the model for the LFP/LTO system at 1C effectively represented the connection between geometry and energy in the extrapolation area, it is desirable to improve the accuracy of the model and confirm the validity of the optimal geometries. As the model exhibited great accuracy for the training data (R^2 of 0.99, as shown in Figure 4A), we suspect that the model slightly overfitted to the training data, which might lead to the decrease in the accuracy in the extrapolation region. On the other hand, as the model captures the relationship between the geometry and energy in the extrapolation region, we assume that only small modifications are necessary for the improvement. Thus, we redeveloped the regression model by

https://doi.org/10.1021/acsphyschemau.4c00039
ACS Phys. Chem Au 2024, 4, 546−554

adding energy data of the optimal geometries in the test data without changing the training data. This treatment adjusts the number of principal components as that number is determined to maximize R^2 of the test data (see Computational Details in the Supporting Information). Indeed, the prediction accuracy of the optimal geometries increased drastically (the averaged error of only 1.7%) at the cost of a very slight reduction of R^2(train.) value, which is 0.986, as shown in Figure S11 in the Supporting Information. Although we reoptimized geometries using this model with AGG-MCTS, we did not find new optimal geometries. Thus, we conclude that geometries (a) − (g) in Figure 4 are the optimal geometries for the LFP/LTO system.

Performance of Optimal Geometries

To investigate the performance of the optimal geometries, theoretical Ragone plots are compared in Figure 6. Associated performance data are summarized in Tables S8 − S13 in the Supporting Information. For comparison, performance data for the conventional parallel plate configuration (PPC) and the optimized geometry for the LMO/GR system (LMO/GR-(OPT)),[24] illustrated in Figure S6 in the Supporting Information, are also included in Tables S8 − S13. Only the data for LMO/GR(OPT) is included in Figure 6 as the energy of PPC is very low.

First, we take a look at the results of the LFP/LTO system. From Table S9, it is clear that the energy of PPC for the LFP/LTO system is much lower than the other systems, indicating use of the thick electrodes is not an effective option to improve the areal energy density. Additionally, the impact of the 3D geometry on energy is significant. Although the Ragone plot does not clearly show the superiority of the optimal geometries over LMO/GR(OPT), their advantage is definitively confirmed in Table S9. At 1C and 2C, all the optimal geometries show greater energy than LMO/GR(OPT). As for 1C, the optimal geometries display from 4% to 9% greater energy than LMO/GR(OPT). For the 2C rate, the superiority of the optimal geometries is more evident, with the energy advantage ranging from 14% to 72%. Among the optimal geometries, geometry (b) demonstrates the best performance at 1C, while geometry (g) shows the best performance for rates other than 1C. The energy of geometry (g) is superior to that of the LMO/GR system by 72%, 14%, and 33% for the 2C, 3C, and 4C rates, respectively.

To investigate the reason why optimal geometries show better performance compared with the LMO/GR(OPT), initial capacity (Q) and averaged internal resistance (R^{ave}) are summarized in Table S10 in the Supporting Information. Overall, the optimal geometries have smaller Q but lower R^{ave}, compared with LMO/GR(OPT). Thus, the lower internal resistance contributes to the greater energy. It is interesting that only the 10 Ω difference between geometry (g) and LMO/GR(OPT) for 4C leads to the significant difference in energy (33%). This means that the internal-resistance difference strongly impacts the battery performance especially when the current density is high.

In the case of the NMC532/GR system, similar to the LPF/LTO system, PPC exhibits much lower energies compared to 3D batteries, as shown in Table S12. The advantage of the optimal geometries over the LMO/GR(OPT) is clear from both the Ragone plot (Figure 6B) and Table S12. From 1C to 6C, the geometry (h) shows the greatest energy, and the geometry (o) for 8C. The advantage of the best geometries over the LMO/GR(OPT) increases with the strength of the current, i.e., the difference is around 7% for 1C and 40% for 8C. When miniaturizing batteries, the energy density at the high current condition is particularly important. Thus, the results indicate that the optimization of electrode geometry is crucial for this system.

Q and R^{ave} of the optimal geometries as well as PPC and LMO/GR(OPT) are summarized in Table S13 for the NMC532/GR system. As is the same with the case for the LFP/LTO system, lower R^{ave} contributes to the greater energy for the optimal geometries compared with the LMO/GR-(OPT). At 8C, although the geometry (o) has around 16% smaller Q compared with the LMO/GR(OPT), the great reduction of R^{ave} (66 Ω) results in 40% greater energy. Again, the internal resistance plays a key role in improving the energy density especially when the current is large.

CONCLUSIONS

In this paper, we propose an automatic 3D battery optimization scheme, the key components of which include our previously proposed automatic geometry generator and the newly developed electrochemistry-based regression models. These models are designed for quickly and accurately predicting areal energy density. To achieve high accuracy with the regression models, we incorporate the nonlinear effect of the electrode/electrolyte interface reaction to evaluate the internal resistance, which is a key feature of the model. This enables the accurate prediction of energies for optimal geometries that lie in the extrapolation region, regardless of the materials and current conditions. In this paper, the accuracy of the regression models is confirmed by comparing predicted energies with those from the continuum simulations. Although we utilized the continuum simulations under crude approximation as a reference, the simulation methods used are known to reproduce experimentally observed discharge curves (hence, energies) well for both conventional[25] and 3D batteries;[32] moreover, optimizations were carried out in the reports. Thus, we believe that our regression models can predict the energies of fabricated batteries as long as the materials parameters are carefully chosen and stable fabrication processes that reproduce battery properties are used. The experimental validation is the main focus of our future work.

To demonstrate the effectiveness of the scheme, we applied it to find the optimal 3D batteries for two kinds of positive electrode/negative electrode pairs, namely, the LFP/LTO and the NMC532/GR systems. These systems were chosen because they are standard combinations but their material properties are distinctly different. Using AGG-MCTS combined with the energy prediction models, we demonstrated for the first time that the optimal geometry changes with the current condition as well as with the combination of electrodes. Notably, the merit of optimization is highlighted under high current conditions, where the optimal geometries showed 30% and 40% greater energy for the LFP/LTO and NMC532/GR systems respectively, compared with the best geometry for the LMO/GR system.

From the results, we conclude that a tailor-made battery is essential for maximizing the performance of specific applications, and our method has the potential to realize such designs. In the field of 3D batteries, a variety of fabrication methods are proposed, and the available materials are strongly limited by the methods. Our approach should play an important role in designing 3D batteries under such limitations.

https://doi.org/10.1021/acsphyschemau.4c00039
ACS Phys. Chem Au 2024, 4, 546−554

■ ASSOCIATED CONTENT

Supporting Information

The Supporting Information is available free of charge at https://pubs.acs.org/doi/10.1021/acsphyschemau.4c00039.

Computational details, supplementary figures and tables (PDF)

Supplemental data related to Figures 4 and 5, which include data to create regression models and generated battery geometries (ZIP)

■ AUTHOR INFORMATION

Corresponding Author

Kaito Miyamoto − *Toyota Central R&D Labs., Inc., Nagakute, Aichi 480-1192, Japan;* orcid.org/0000-0003-1827-5494; Phone: +81-561-71-7973; Email: kaito@mosk.tytlabs.co.jp

Complete contact information is available at: https://pubs.acs.org/10.1021/acsphyschemau.4c00039

Notes

The author declares no competing financial interest.

■ REFERENCES

(1) Swan, M. Sensor mania! the internet of things, wearable computing, objective metrics, and the quantified self 2.0. *J. Sens. Actuator Netw.* **2012**, *1*, 217−253.
(2) Hur, J. I.; Smith, L. C.; Dunn, B. High areal energy density 3D lithium-ion microbatteries. *Joule* **2018**, *2*, 1187−1201.
(3) Dudney, N. J. Thin film micro-batteries. *Electrochem. Soc. Interface* **2008**, *17*, 44.
(4) Pikul, J. H.; Ning, H. Powering the Internet of Things. *Joule* **2018**, *2*, 1036−1038.
(5) Hung, C.-H.; Allu, S.; Cobb, C. L. Modeling current density non-uniformities to understand high-rate limitations in 3D interdigitated lithium-ion batteries. *J. Electrochem. Soc.* **2021**, *168*, 100512.
(6) Long, J. W.; Dunn, B.; Rolison, D. R.; White, H. S. 3D Architectures for Batteries and Electrodes. *Adv. Energy Mater.* **2020**, *10*, 2002457.
(7) Long, J. W.; Dunn, B.; Rolison, D. R.; White, H. S. Three-dimensional battery architectures. *Chem. Rev.* **2004**, *104*, 4463−4492.
(8) Sha, M.; Zhao, H.; Lei, Y. Updated Insights into 3D Architecture Electrodes for Micropower Sources. *Adv. Mater.* **2021**, *33*, 2103304.
(9) Ning, H.; Pikul, J. H.; Zhang, R.; Li, X.; Xu, S.; Wang, J.; Rogers, J. A.; King, W. P.; Braun, P. V. Holographic patterning of high-performance on-chip 3D lithium-ion microbatteries. *Proc. Natl. Acad. Sci. U.S.A.* **2015**, *112*, 6573−6578.
(10) Sun, P.; Li, X.; Shao, J.; Braun, P. V. High-Performance Packaged 3D Lithium-Ion Microbatteries Fabricated Using Imprint Lithography. *Adv. Mater.* **2021**, *33*, 2006229.
(11) Zhang, F.; Wei, M.; Viswanathan, V. V.; Swart, B.; Shao, Y.; Wu, G.; Zhou, C. 3D printing technologies for electrochemical energy storage. *Nano Energy* **2017**, *40*, 418−431.
(12) Wei, M.; Zhang, F.; Wang, W.; Alexandridis, P.; Zhou, C.; Wu, G. 3D direct writing fabrication of electrodes for electrochemical storage devices. *J. Power Sources* **2017**, *354*, 134−147.
(13) Zhu, C.; Liu, T.; Qian, F.; Chen, W.; Chandrasekaran, S.; Yao, B.; Song, Y.; Duoss, E. B.; Kuntz, J. D.; Spadaccini, C. M.; et al. 3D printed functional nanomaterials for electrochemical energy storage. *Nano Today* **2017**, *15*, 107−120.
(14) Mazor, H.; Golodnitsky, D.; Burstein, L.; Gladkich, A.; Peled, E. Electrophoretic deposition of lithium iron phosphate cathode for thin-film 3D-microbatteries. *J. Power Sources* **2012**, *198*, 264−272.
(15) Pikul, J. H.; Zhang, H. G.; Cho, J.; Braun, P. V.; King, W. P. High-power lithium ion microbatteries from interdigitated three-dimensional bicontinuous nanoporous electrodes. *Nat. Commun.* **2013**, *4*, 1732.
(16) Sun, K.; Wei, T.-S.; Ahn, B. Y.; Seo, J. Y.; Dillon, S. J.; Lewis, J. A. 3D printing of interdigitated Li-Ion microbattery architectures. *Adv. Mater.* **2013**, *25*, 4539−4543.
(17) Fu, K.; Wang, Y.; Yan, C.; Yao, Y.; Chen, Y.; Dai, J.; Lacey, S.; Wang, Y.; Wan, J.; Li, T.; et al. Graphene oxide-based electrode inks for 3D-printed lithium-ion batteries. *Adv. Mater.* **2016**, *28*, 2587−2594.
(18) Izumi, A.; Sanada, M.; Furuichi, K.; Teraki, K.; Matsuda, T.; Hiramatsu, K.; Munakata, H.; Kanamura, K. Development of high capacity lithium-ion battery applying three-dimensionally patterned electrode. *Electrochim. Acta* **2012**, *79*, 218−222.
(19) Horowitz, Y.; Strauss, E.; Peled, E.; Golodnitsky, D. How to Pack a Punch−Why 3D Batteries are Essential. *Isr. J. Chem.* **2021**, *61*, 38−50.
(20) Lyu, Z.; Lim, G. J.; Koh, J. J.; Li, Y.; Ma, Y.; Ding, J.; Wang, J.; Hu, Z.; Wang, J.; Chen, W.; et al. Design and manufacture of 3D-printed batteries. *Joule* **2021**, *5*, 89−114.
(21) McKelvey, K.; Cabré, M. B.; Paiva, A. E. Continuum Simulations for Microscale 3D Batteries. *Curr. Opin. Electrochem.* **2020**, *21*, 76−83.
(22) Miyamoto, K.; Sasaki, T.; Nishi, T.; Itou, Y.; Takechi, K. 3D-microbattery architectural design optimization using automatic geometry generator and transmission-line model. *iScience* **2020**, *23*, 101317.
(23) Miyamoto, K.; Broderick, S.; Rajan, K. Three-dimensional microbattery design via an automatic geometry generator and machine-learning-based performance simulator. *Cell Rep. Phys. Sci.* **2021**, *2*, 100504.
(24) Miyamoto, K.; Broderick, S. R.; Rajan, K. Data-driven optimization of 3D battery design. *J. Power Sources* **2022**, *536*, 231473.
(25) Doyle, M.; Newman, J.; Gozdz, A. S.; Schmutz, C. N.; Tarascon, J.-M. Comparison of modeling predictions with experimental data from plastic lithium ion cells. *J. Electrochem. Soc.* **1996**, *143*, 1890−1903.
(26) Wang, Z.; Ni, J.; Li, L.; Lu, J. Theoretical simulation and modeling of three-dimensional batteries. *Cell Rep. Phys. Sci.* **2020**, *1*, 100078.
(27) Zadin, V.; Kasemägi, H.; Aabloo, A.; Brandell, D. Modelling electrode material utilization in the trench model 3D-microbattery by finite element analysis. *J. Power Sources* **2010**, *195*, 6218−6224.
(28) Zadin, V.; Brandell, D.; Kasemägi, H.; Aabloo, A.; Thomas, J. O. Finite element modelling of ion transport in the electrolyte of a 3D-microbattery. *Solid State Ionics* **2011**, *192*, 279−283.
(29) Zadin, V.; Brandell, D. Modelling polymer electrolytes for 3D-microbatteries using finite element analysis. *Electrochim. Acta* **2011**, *57*, 237−243.
(30) Priimägi, P.; Brandell, D.; Srivastav, S.; Aabloo, A.; Kasemägi, H.; Zadin, V. Optimizing the design of 3D-pillar microbatteries using finite element modelling. *Electrochim. Acta* **2016**, *209*, 138−148.
(31) Miranda, D.; Costa, C.; Almeida, A.; Lanceros-Méndez, S. Computer simulation evaluation of the geometrical parameters affecting the performance of two dimensional interdigitated batteries. *J. Electroanal. Chem.* **2016**, *780*, 1−11.
(32) Pikul, J. H.; Braun, P. V.; King, W. P. Performance modeling and design of ultra-high power microbatteries. *J. Electrochem. Soc.* **2017**, *164*, E3122−E3131.
(33) Li, J.; Liang, X.; Panat, R.; Park, J. Enhanced Battery Performance through Three-Dimensional Structured Electrodes: Experimental and Modeling Study. *J. Electrochem. Soc.* **2018**, *165*, A3566−A3573.
(34) Zadin, V.; Brandell, D.; Kasemägi, H.; Lellep, J.; Aabloo, A. Designing the 3D-microbattery geometry using the level-set method. *J. Power Sources* **2013**, *244*, 417−428.
(35) Miyamoto, K. *Multiscale Simulations for Electrochemical Devices*; CRC Press, 2020; pp 25−55.
(36) Vijay, P.; Tadé, M. O. Improved approximation for the butler-volmer equation in fuel cell modelling. *Comput. Chem. Eng.* **2017**, *102*, 2−10.
(37) Wang, F.; Tang, M. A Quantitative Analytical Model for Predicting and Optimizing the Rate Performance of Battery Cells. *Cell Rep. Phys. Sci.* **2020**, *1*, 100192.